Original Paper

Effects of acid−rock reaction on physical properties during CO$_2$-rich industrial waste gas (CO$_2$-rich IWG) injection in shale reservoirs

Yi-Fan Wang [a, b], Jing Wang [a, b, *], Hui-Qing Liu [a, b], Xiao-Cong Lv [a, b], Ze-Min Ji [c]

[a] National Key Laboratory of Petroleum Resources and Engineering, China University of Petroleum, Beijing, 102249, China
[b] MOE Key Laboratory of Petroleum Engineering, China University of Petroleum, Beijing, 102249, China
[c] Research Institute of Exploration and Development, PetroChina, Beijing, 100083, China

A R T I C L E   I N F O

A B S T R A C T

"Carbon peaking and carbon neutrality" is an essential national strategy, and the geological storage and utilization of CO$_2$ is a hot issue today. However, due to the scarcity of pure CO$_2$ gas sources in China and the high cost of CO$_2$ capture, CO$_2$-rich industrial waste gas (CO$_2$-rich IWG) is gradually emerging into the public's gaze. CO$_2$ has good adsorption properties on shale surfaces, but acidic gases can react with shale, so the mechanism of the CO$_2$-rich IWG−water−shale reaction and the change in reservoir properties will determine the stability of geological storage. Therefore, based on the mineral composition of the Longmaxi Formation shale, this study constructs a thermodynamic equilibrium model of water−rock reactions and simulates the regularity of reactions between CO$_2$-rich IWG and shale minerals. The results indicate that CO$_2$ consumed 12% after reaction, and impurity gases in the CO$_2$-rich IWG can be dissolved entirely, thus demonstrating the feasibility of treating IWG through water−rock reactions. Since IWG inhibits the dissolution of CO$_2$, the optimal composition of CO$_2$-rich IWG is 95% CO$_2$ and 5% IWG when CO$_2$ geological storage is the main goal. In contrast, when the main goal is the geological storage of total CO$_2$-rich IWG or impurity gas, the optimal CO$_2$-rich IWG composition is 50% CO$_2$ and 50% IWG. In the CO$_2$-rich IWG−water−shale reaction, temperature has less influence on the water−rock reaction, while pressure is the most important parameter. SO$_2$ has the greatest impact on water−rock reaction in gas. For minerals, clay minerals such as illite and montmorillonite had a significant effect on water−rock reaction. The overall reaction is dominated by precipitation and the volume of the rock skeleton has increased by 0.74 cm^3, resulting in a decrease in shale porosity, which enhances the stability of CO$_2$ geological storage to some extent. During the reaction between CO$_2$-rich IWG−water−shale at simulated temperatures and pressures, precipitation is the main reaction, and shale porosity decreases. However, as the reservoir water content increases, the reaction will first dissolve and then precipitate before dissolving again. When the water content is less than 0.0005 kg or greater than 0.4 kg, it will lead to an increase in reservoir porosity, which ultimately reduces the long-term geological storage stability of CO$_2$-rich IWG.

1. Introduction

According to statistics from the International Energy Agency, global CO$_2$ emissions related to energy reached more than 36.8 billion tons in 2022, an increase of 0.9% compared to 2021, leading to an exacerbation of the greenhouse effect (IEA., 2022). Thus,

reducing greenhouse gas emissions has become a pressing issue. Currently, CO$_2$ geological storage is widely recognized as the preferred option to achieve this goal (Hu et al., 2019; Fatah et al., 2020; Liao et al., 2022; Yuan et al., 2022; Li et al., 2023; Wang, 2023). In China, pure CO$_2$ gas sources are relatively scarce (Song et al., 2023; Zou et al., 2023), and therefore, industrial waste gases rich in CO$_2$ have gradually attracted attention. More than half of the total CO$_2$ emissions from the use of fossil fuels worldwide are attributed to the large fixed emission sources in the energy and industrial sectors (Li et al., 2010). Industrial waste gases are the

most significant source of CO_2 emissions (Ghayur et al., 2019; Teng et al., 2019; Zhang et al., 2022). However, the problem of dealing with impurity gases (such as CO, SO_2, NO_2, H_2S, HF, O_2, etc.) in the waste gases urgently needs to be solved. Therefore, achieving low-cost and efficient carbon storage is crucial, and the issue of how to treat impurities in the CO_2-rich IWG at a lower cost is of paramount importance.

Due to the excellent adsorption capacity and large specific surface area for CO_2, shale is considered an excellent site for carbon storage (Liu et al., 2016; Merey and Sinayuc, 2016; Zhou et al., 2019; Fatah et al., 2020). Existing studies have shown that injecting CO_2 into shale gas reservoirs can not only increase the recovery rate of shale gas but also achieve effective and stable carbon storage (Middleton et al., 2015; Rezaee et al., 2017; Lyu et al., 2018; Song et al., 2018, 2019; Hadian and Rezaee, 2019; Wang et al., 2019; Lang et al., 2021). Acidic gases such as CO_2, SO_2, NO_2, H_2S, and HF, when dissolved in water, can also undergo acid—rock reactions with rock minerals to form mineral precipitates, which can be permanently stored underground (Aminu et al., 2018; Zhou et al., 2018; Sturmer et al., 2020; Yuan et al., 2021; Pearce et al., 2022; Turner et al., 2022). Therefore, CO_2-rich IWG can be directly injected into shale reservoirs, which not only treats the impurities in industrial waste gases but also achieves carbon storage, greatly reducing the cost (Yuan et al., 2021; Wang et al., 2022a, 2022b). However, the geochemical interactions between CO_2-rich IWG and shale are not yet well understood. The water—rock reactions can affect gas dissolution and mineral dissolution/precipitation (Ilgen et al., 2018; Zhu et al., 2019; Fatah et al., 2021), significantly affecting reservoir properties, increasing the risk of CO_2-rich IWG leakage (Liu et al., 2016), and posing significant safety hazards due to the presence of toxic gases such as CO and H_2S. Therefore, it is necessary to conduct in-depth research on the reaction mechanisms of CO_2-rich IWG—water—shale and evaluate their impact on reservoir properties.

Numerous experimental results have shown that CO_2 dissolved in formation water forms carbonic acid, which reacts with various clay minerals and carbonate minerals in shale formations, resulting in significant changes in shale mineral composition (Yin et al., 2016; Ao et al., 2017; Rezaee et al., 2017; Pan et al., 2018; Hui et al., 2019; Fatah et al., 2021, 2022). In recent years, some scholars have conducted experimental studies of the CO_2—water—shale interactions to evaluate the impact of CO_2 injection on the properties of shale reservoirs and to demonstrate the feasibility of shale formations as a geologic CO_2 storage site (Hadian and Rezaee, 2019; Hui et al., 2019; Bhuiyan et al., 2020; Cheng et al., 2020; Dai et al., 2020; Fatah et al., 2020, 2021; Pan et al., 2020; Qin et al., 2020; Zhou et al., 2020). Although experimental studies allow us to control essential parameters such as pressure and temperature and provide a good assessment of the direction of CO_2—water—shale interactions (Koukouzas et al., 2018), mineral dissolution and precipitation processes are slow and complex (Yang et al., 2020). Therefore, numerical simulation of water—rock reactions can better clarify the complex mechanism of CO_2—water—shale interactions and study the mineral evolution throughout the entire geological timescale of the CO_2 geologic storage process (Zhang et al., 2020a, 2020b).

Many existing results mainly focus on the geologic storage of CO_2 in traditional formations such as deep saline formations and sandstone formations. There are few studies of shale formations, and almost no studies of the interaction between CO_2-rich IWG and shale minerals. Therefore, the aim of this study is to investigate the interactions between CO_2-rich IWG (including CO_2, CO, SO_2, NO_2, H_2S, and HF) and shale, reveal the mechanism of the CO_2-rich IWG—water—shale mineral reactions, and obtain the regularity of

the impact of water—rock reactions on the physical properties of shale reservoirs. In this study, a core-scale model was established to study the thermodynamic equilibrium state of the CO_2-rich IWG—water—shale mineral chemical system. The accuracy of the model was verified by comparing it with the results of existing literature (Klajmon et al., 2017).

2. Numerical implementation

2.1. Theoretical approach

The fundamental principles of geochemical modeling are based on three main processes: thermodynamic equilibrium, reaction kinetics, and mass transport processes. This study focuses on simulating the thermodynamic equilibrium between CO_2-rich IWG (considering CO_2, CO, SO_2, NO_2, H_2S, and HF), water, and shale minerals. A single-phase, one-dimensional reactive transport model was established to simulate thermodynamic equilibrium models under specific reservoir conditions. In terms of chemical equilibrium thermodynamics, this model combines three equations: mass action equations, mass balance equations, and charge balance equations to establish a thermodynamic equilibrium model. This model results in a series of nonlinear algebraic equations, which are solved using the Newton-Raphson iteration method (Bethke, 1996). The subsequent section elaborates in detail on the thermodynamic equilibrium model of the chemical reactions between CO_2-rich IWG—water—shale minerals.

When a chemical system reaches thermodynamic equilibrium, all possible chemical reactions within the system have forward and backward reaction rates that are equal, meaning that the system has reached a stable state with no net production or consumption of chemical species. Therefore, the equilibrium conditions of each chemical reaction can be used to calculate the equilibrium state of the entire chemical system. In the field of hydrogeochemistry, the most commonly used equilibrium condition for chemical reactions is the law of mass action. The mass action equation for aqueous solutions is generally expressed as follows:

$$K_i = a_i \prod_m^{M_{aq}} a_m^{-c_{m,i}}, \tag{1}$$

where K_i represents the equilibrium constant of the chemical reaction, which is temperature-dependent; a_i represents the activity of species i in the aqueous solution; M_{aq} is the number of master species in the aqueous solution of the reaction; $c_{m,i}$ represents the stoichiometric coefficient of the master species m in species i, which can be a positive or negative value. In this model, the terms on the right side of the equilibrium reaction are assigned negative values. In contrast, the terms on the left side are assigned positive values. The total amount of species i in the aqueous solution can be obtained from the mass action expression:

$$n_i = m_i W_{aq} = \frac{a_i}{\gamma_i} W_{aq} = K_i W_{aq} \frac{\prod_m^{M_{aq}} a_m^{c_{m,i}}}{\gamma_i}, \tag{2}$$

where n_i represents the total number of moles of species i in the aqueous solution; m_i represents the molar concentration of species i in the aqueous solution; W_{aq} represents the mass of solvent water in the aqueous solution; γ_i represents the activity coefficient of species i in the aqueous solution. The activity coefficient of a species in the aqueous solution is defined by the Davies equation (Davies, 1951):

$$\log \gamma_i = -A z_i^2 \left(\frac{\sqrt{\mu}}{1+\sqrt{\mu}} - 0.3\mu \right), \tag{3}$$

where z_i represents the ion charge number of species i in the aqueous solution; A is a constant that is only related to temperature; μ represents the ionic strength of the aqueous solution, which is defined by the following formula:

$$\mu = \frac{1}{2} \sum_i^{N_{aq}} z_i^2 \frac{n_i}{W_{aq}}, \tag{4}$$

where N_{aq} is the total number of species in the aqueous solution, this model describes the equilibrium state by the law of mass action. Thermodynamic equilibrium is reached when the system satisfies the mass action equation simultaneously. However, the mass action equation alone cannot be solved, and a series of nonlinear equations must be derived by incorporating the mole number equations of substances into the mass balance and charge balance equations, which are ultimately solved using the Newton-Raphson iterative method.

In the equilibrium model of chemical reactions in CO_2-rich IWG−water−shale minerals, not only the equilibrium of chemical reactions in the aqueous solution must be considered, but also the equilibrium between the water phase and other pure phases, including minerals with fixed composition and gases with fixed partial pressure. This model allows for multiple pure phases (referred to as pure phase combinations) to equilibrate with the water phase. According to Gibbs' phase rule, the activity of pure phases is assumed to be 1.0. The activity of the water phase is then calculated using the approximate value of Raoult's law (Garrels and Christ, 1965):

$$a_{H_2O} = 1 - 0.017 \sum_i^{N_{aq}} \frac{n_i}{W_{aq}}. \tag{5}$$

This model uses dissolution reactions to describe the interactions between each pure phase and the aqueous phase. Thus pure phases are located on the left-hand side of the chemical equation. The equilibrium condition of the pure phase dissolution reaction can be expressed by the following mass action equation:

$$K_p = \prod_m^{M_{aq}} a_m^{c_{m,p}}, \tag{6}$$

where K_p is the equilibrium constant for the pure phase dissolution reaction; and $c_{m,p}$ is the stoichiometric coefficient of the master species m in the dissolution reaction. The saturation index SI_p of a mineral is defined as

$$SI_p = \log \prod_m^{M_{aq}} a_m^{c_{m,p}}. \tag{7}$$

The function used in this model to describe phase equilibrium is

$$f_p = \left(\ln K_p + SI_{p,\text{target}} \ln 10 \right) - \prod_m^{M_{aq}} c_{m,p} \ln a_m, \tag{8}$$

where $SI_{p,\text{target}}$ is the target saturation index of the mineral, which is specified by the user and indicates whether the mineral is oversaturated, at equilibrium, or undersaturated with respect to the solution, generally set to 0 by default. For gases with fixed partial pressures, $SI_{p,\text{target}}$ is the logarithm of the gas component partial pressure.

This model employs element balance equations to describe the overall mass balance in the system, which is manifested as the total moles of elements in the system being the sum of the moles initially present in the pure phases and aqueous phase, as represented by the following function:

$$f_m = T_m - \sum_p^{N_p} b_{m,p} n_p - \sum_i^{N_{aq}} b_{m,i} n_i, \tag{9}$$

where the value of function f_m is zero when the system reaches mass balance; T_m is the total moles of each element in the system; N_p is the number of phases in the pure phase combination; n_p is the moles of each phase in the pure phase combination; $b_{m,p}$ and $b_{m,i}$ are the moles of element m per mole of species in the pure phase or per mole of species in the aqueous solution, respectively.

In the initial solution calculations, this model adjusts the pH of the aqueous solution using the charge balance equation to make the solution electrically neutral or to calculate the activity of the master species in the aqueous solution, thus obtaining the total concentration of each element. The charge balance equation is necessary to calculate the pH value in the batch reaction. In actual solutions, the sum of anions and cations must be zero. However, computational errors in chemical equilibrium calculations often lead to charge imbalances in the calculated results. If the initial solution calculation results in a charge imbalance, the pH value needs to be adjusted in subsequent batch reactions to maintain the same charge imbalance. In each initial solution calculation and in each batch reaction step, the following formula is used to calculate the charge imbalance in the aqueous solution:

$$T_{z,q} = \sum_i^{N_{aq}} z_i n_i, \tag{10}$$

where $T_{z,q}$ represents the charge imbalance in the aqueous solution. Therefore, in the process of chemical equilibrium simulation, at the calculation of the initial solution and the beginning of each batch reaction step, the charge imbalance of the entire system is defined as follows:

$$T_z = \sum_q^{Q} \alpha_q T_{z,q}, \tag{11}$$

where T_z is the charge imbalance of the entire chemical system; Q is the quantity of water phase mixed in batch reaction steps; and α_q is the mixing fraction of water phase q. Thus, the charge balance equation for the entire chemical system is

$$f_z = T_z - \sum_i^{N_{aq}} z_i n_i, \tag{12}$$

where the system reaches charge balance when the value of function f_z is zero, when the combination of pure phase, aqueous phase, and the master species in the aqueous solution of the entire system satisfies the mass action equation, and all functions related to the specific equilibrium calculation are equal to zero, the entire system reaches an equilibrium state. This model uses the Newton-Raphson method to solve the zero points of each function. With this method, each function is differentiated with respect to each main unknown quantity to form a Jacobian matrix. A series of linear equations can be formed from the Jacobian matrix, and the iterative solution of the continuous linear equation set can be used to obtain the solution to the nonlinear equations, ultimately obtaining the

state of the entire system when it reaches thermodynamic equilibrium. In addition, the theory as well as the equations used in this model have been extensively validated to simulate the thermodynamic equilibrium state of chemical systems accurately and efficiently with excellent reliability.

2.2. Model concepts

The mineral composition and chemical composition of the core samples used in the equilibrium reaction simulation are shown in Table 1. The shale mineral composition is based on the mineral composition of the Longmaxi shale from Sichuan Basin (Dong et al., 2018; Wang et al., 2021; Sun et al., 2023), where the content of quartz, carbonate rocks dominated by calcite, and clay minerals (illite and montmorillonite) is relatively high, all ranging from 20% to 30%, and there are small amounts of feldspar and pyrite.

A simplified one-dimensional model of the water−rock reaction at the rock core scale was constructed to simulate the equilibrium of CO_2-rich IWG−water−shale interactions during the geological storage stage. The equilibrium model was performed under isothermal conditions of 70 °C, assuming injection of 1.0 mol of CO_2-rich IWG (with a gas composition of 75% CO_2, 5% CO, 5% NO_2, 5% SO_2, 5% H_2S, and 5% HF) into shale pore spaces at a pressure of 20 MPa, with a water−rock ratio of 100 g:50 mL. The temperature and pressure conditions were set based on shallow shale reservoirs in the Longmaxi Formation in the Sichuan Basin. The mathematical principles of the equilibrium reaction model were based on the thermodynamic data compiled by the Lawrence Livermore National Laboratory. The equilibrium model used a set of chemical reactions to simulate the thermodynamic equilibrium between CO_2-rich IWG dissolution in water and the interaction between CO_2-rich IWG and shale minerals. The chemical reactions involved in the equilibrium model are shown in Table 2. These chemical reactions control the interactions between various substances under equilibrium conditions and the dissolution and precipitation of minerals.

2.3. Model validation

This water−rock reaction model was compared and validated against data from Klajmon et al. (2017) to ensure its accuracy in the simulating mineral dissolution/precipitation in the chemical reactions between CO_2-rich IWG−water−shale. The existing experimental research data are mainly based on CO_2−water−sandstone reaction, and the experimental data of CO_2−water−shale reaction are relatively few at present. Since the mineral components of sandstone and the reaction equations have some similarity with shale, we simulated the CO_2−clayey sandstone reaction to verify the accuracy of the model of CO_2−water−shale reaction. This study investigated the interaction between supercritical CO_2 and clayey

sandstone under a temperature of 43 °C and a pressure of 80 atm. By establishing a model with the same simulation parameters (mineral composition, formation water composition, pressure, and temperature), the amount of mineral dissolution or precipitation after the reaction was compared to verify the accuracy of the model. The comparison results, as shown in Fig. 1, indicated that the difference between the two was not significant. Therefore, it is believed that this water−rock reaction model can accurately simulate the CO_2-rich IWG−water−shale reactions. In addition, compared to Klajmon model (Klajmon et al., 2017), the advantage of this model is the use of widely validated theories as well as equations that can accurately and efficiently simulate the thermodynamic equilibrium state of the mixed gas−water−rock reaction.

3. Results and discussion

3.1. Reaction regularity and mechanism of CO_2-rich IWG−water−shale minerals

3.1.1. Reaction regularity of single gas−water−shale minerals

The thermodynamic equilibrium results of each CO_2-rich IWG−water−shale minerals are shown in Fig. 2. The results indicate that under the given temperature and pressure conditions, the amount of CO_2 decreases from 1.0 mol to 0.81 mol after reaction, ultimately consuming 19% of the initial CO_2 amount. It can be seen that the addition of various industrial waste gases suppresses the dissolution of CO_2. CO, NO_2, SO_2, and HF, were completely consumed and produced a certain amount of CO_2. H_2S gas, due to its low solubility, dissolved in water by 0.61 mol, without generating any CO_2. Regarding the shale minerals, the reaction with CO_2 and each individual industrial waste gas resulted in the complete dissolution of albite, illite, and montmorillonite and the precipitation of a substantial amount of quartz. In the case of other minerals, the reaction results of CO_2 and CO were analogous, both indicating the partial dissolution of calcite, precipitation of dolomite, K-feldspar, and secondary minerals such as kaolinite and dawsonite. The outcomes of the reaction of H_2S gas with the former two were not significantly different, except for the absence of a secondary mineral of dawsonite at the end. The solubility of NO_2 and SO_2 in water generates strong acids like nitric acid and sulfurous acid (Pearce et al., 2016; Turner et al., 2022), respectively, and the reaction ultimately results in more mineral dissolution. The NO_2−water−rock reaction ultimately led to the complete dissolution of calcite and pyrite and partial dissolution of dolomite, with no secondary mineral of dawsonite being formed, but rather a precipitation of alunite. The water−rock reaction of SO_2 ultimately resulted in the complete dissolution of calcite, dolomite, and K-feldspar, with only alunite being generated in the secondary minerals. The reaction outcome of HF gas showed the complete dissolution of K-feldspar, partial dissolution of calcite, and precipitation of dolomite, with no

Table 1
Mineral content and geochemical data of the shale samples.

Mineral	Chemical formula	Molecular weight, g/mol	Mass fraction, %	Amount of substance, mol
Quartz	SiO_2	60	22.5	0.375
Calcite	$CaCO_3$	100	29.6	0.296
Dolomite	$CaMg(CO_3)_2$	184	4.5	0.0245
Albite	$NaAlSi_3O_8$	262	7.4	0.0282
K-feldspar	$KAlSi_3O_8$	278	6.6	0.0237
Illite	$K_{0.6}Mg_{0.25}Al_{2.3}Si_{3.5}O_{10}(OH)_2$	383.5	16.9	0.0441
Montmor-Ca	$Ca_{0.165}Mg_{0.33}Al_{1.67}Si_4O_{10}(OH)_2$	365.61	10	0.0274
Pyrite	FeS_2	120	2.5	0.0208
Kaolinite	$Al_2Si_2O_5(OH)_4$	258	0	0
Dawsonite	$NaAlCO_3(OH)_2$	144	0	0
Alunite	$KAl_3(OH)_6(SO_4)_2$	414	0	0

Table 2
Chemical reactions for the thermodynamic equilibrium model.

| Pure phase	Reaction	log$K$
CO_2	$CO_2 + H_2O = H^+ + HCO_3^-$	−7.8136
Calcite	$CaCO_3 + H^+ = Ca^{2+} + HCO_3^-$	1.8487
Dolomite	$CaMg(CO_3)_2 + 2H^+ = Ca^{2+} + Mg^{2+} + 2HCO_3^-$	2.5135
Albite	$NaAlSi_3O_8 + 4H^+ = Na^+ + Al^{3+} + 2H_2O + 3SiO_2$	2.7645
K-feldspar	$KAlSi_3O_8 + 4H^+ = K^+ + Al^{3+} + 2H_2O + 3SiO_2$	−0.2753
Illite	$K_{0.6}Mg_{0.25}Al_{2.3}Si_{3.5}O_{10}(OH)_2 + 8H^+ = 0.6K^+ + 0.25Mg^{2+} + 2.3Al^{3+} + 5H_2O + 3.5SiO_2$	9.0260
Montmor-Ca	$Ca_{0.165}Mg_{0.33}Al_{1.67}Si_4O_{10}(OH)_2 + 6H^+ = 0.165Ca^{2+} + 0.33Mg^{2+} + 1.67Al^{3+} + 4H_2O + 4SiO_2$	2.4952
Pyrite	$FeS_2 + H_2O = 0.25H^+ + 0.25SO_4^{2-} + Fe^{2+} + 1.75HS^-$	−24.6534
Kaolinite	$Al_2Si_2O_5(OH)_4\ 6H^+ = 2Al^{3+} + 5H_2O + 2SiO_2$	6.8101
Dawsonite	$NaAlCO_3(OH)_2 + 3H^+ = Na^+ + Al^{3+} + HCO_3^- + 2H_2O$	4.3464
Alunite	$KAl_3(OH)_6(SO_4)_2 + 6H^+ = K^+ + 3Al^{3+} + 2SO_4^{2-} + 6H_2O$	−0.3479
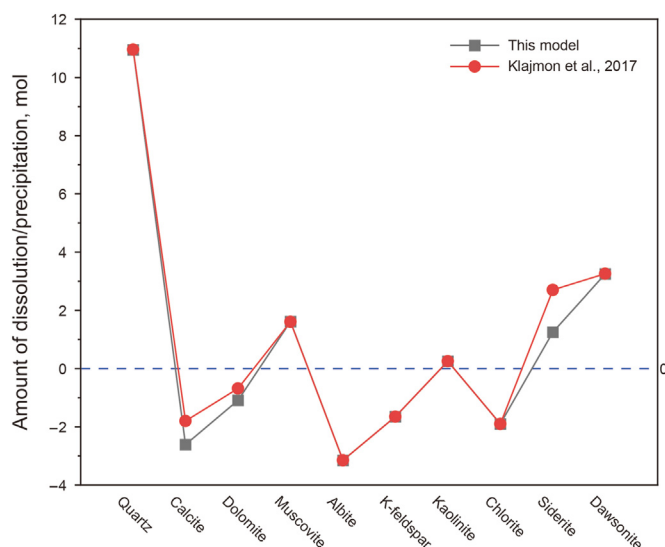
Fig. 1. Validation of this model with literature.

secondary mineral being formed at the end.

The thermodynamic equilibrium results of each CO_2-rich IWG−water−shale minerals vary with temperature, as shown in Fig. 3. The results indicate that, under the simulated temperature and pressure conditions, CO, NO_2, SO_2, and HF can all dissolve completely. The solubility of CO_2 and H_2S gases decreases as the temperature increases, with H_2S having a significantly higher solubility than CO_2 under the same conditions. As for shale minerals, in general, high temperatures inhibit the continuous progress of water−rock reactions. For example, as the temperature increases, the solubility of CO_2 on K-feldspar decreases, and the amount of reaction product quartz also decreases accordingly. The ability of H_2S gas to dissolve calcite also decreases with increasing temperature.

The thermodynamic equilibrium results of each CO_2-rich IWG−water−shale minerals with different pressures are shown in Fig. 4. The results indicate that within the simulated pressure and temperature ranges, CO, NO_2, SO_2, and HF, were able to dissolve completely. The solubility of CO_2 and H_2S gases increases as the pressure increases. With regard to shale minerals, increasing pressure promotes water−rock reactions. For example, as the pressure increases, the dissolution of CO_2 in K-feldspar increases, and the amount of quartz produced also increases accordingly.

Fig. 5 displays the thermodynamic equilibrium results between each CO_2-rich IWG−water−shale minerals with respect to the gas concentration. The results indicate that CO, NO_2, SO_2, and HF gases can all be completely dissolved under simulated gas concentrations

and temperature conditions. CO_2 and H_2S gases can be completely dissolved at low concentrations but gradually reach a state of dissolution equilibrium as the concentration increases. With increasing acidic gas concentration, many shale minerals tend to undergo precipitation before dissolution. For instance, calcite, K-feldspar, kaolinite, and alunite all undergo precipitation before dissolution until complete dissolution is achieved with the increase in SO_2 gas concentration. Most of the existing studies of water−rock reactions are on CO_2 or a mixture of CO_2 and a single waste gas, and there is a lack of studies of the water−rock reactions of a single waste gas with shale minerals (Farquhar et al., 2015; Pearce et al., 2016; Fatah et al., 2021, 2022; Turner et al., 2022). Combining this part of the study can provide a more comprehensive analysis of the reaction mechanism between CO_2-rich IWG and shale minerals.

3.1.2. Reaction mechanism of single gas−water−shale minerals

The gas−water−rock interactions of CO_2, CO, NO_2, SO_2, H_2S, and HF are essentially characterized by the dissolution of gases in water to form acids, which release H^+ cations that react with shale minerals to produce acid−rock reactions. As a result, shale minerals undergo a sequence of reactions upon dissolution in water, ultimately leading to precipitation. This is consistent with the findings of existing studies (Koukouzas et al., 2018; Liu et al., 2019; Zhu et al., 2019), therefore the final reaction outcomes are closely linked to gas solubility and acidity of the acids produced. Among the aforementioned gases, SO_2, NO_2, and HF exhibit high solubility and generate sulfurous acid, nitric acid, and hydrofluoric acid, respectively, upon dissolution in water, which are strong acids. Therefore, calcite, albite, illite, and montmorillonite are entirely dissolved upon reacting with shale minerals, whereas quartz precipitates. Nitric acid leads to pyrite decomposition and the formation of alunite containing SO_4^{2-}. As HF molecules possess high polarity, they readily dissolve in water, yielding hydrogen fluoride. Despite being a weak acid, hydrofluoric acid is highly corrosive and reacts with quartz to produce silicon tetrafluoride. Consequently, high concentrations of HF gas can dissolve quartz minerals after reacting with shale minerals. In contrast to the aforementioned gases, CO_2 and H_2S exhibit weaker solubility in water and yield weak acids upon dissolution in water. Consequently, only albite, illite, and montmorillonite are entirely dissolved after reacting with shale minerals, while quartz and some secondary minerals are produced. As CO is challenging to dissolve in water, it undergoes oxidation reactions primarily to form CO_2. Thus, the reaction outcomes between CO gas and shale minerals are highly similar to those of CO_2 and shale minerals.

3.1.3. Reaction regularity of mixed gas−water−shale minerals

The thermodynamic equilibrium results between CO_2-rich IWG−water−shale minerals are shown in Fig. 6. The simulation
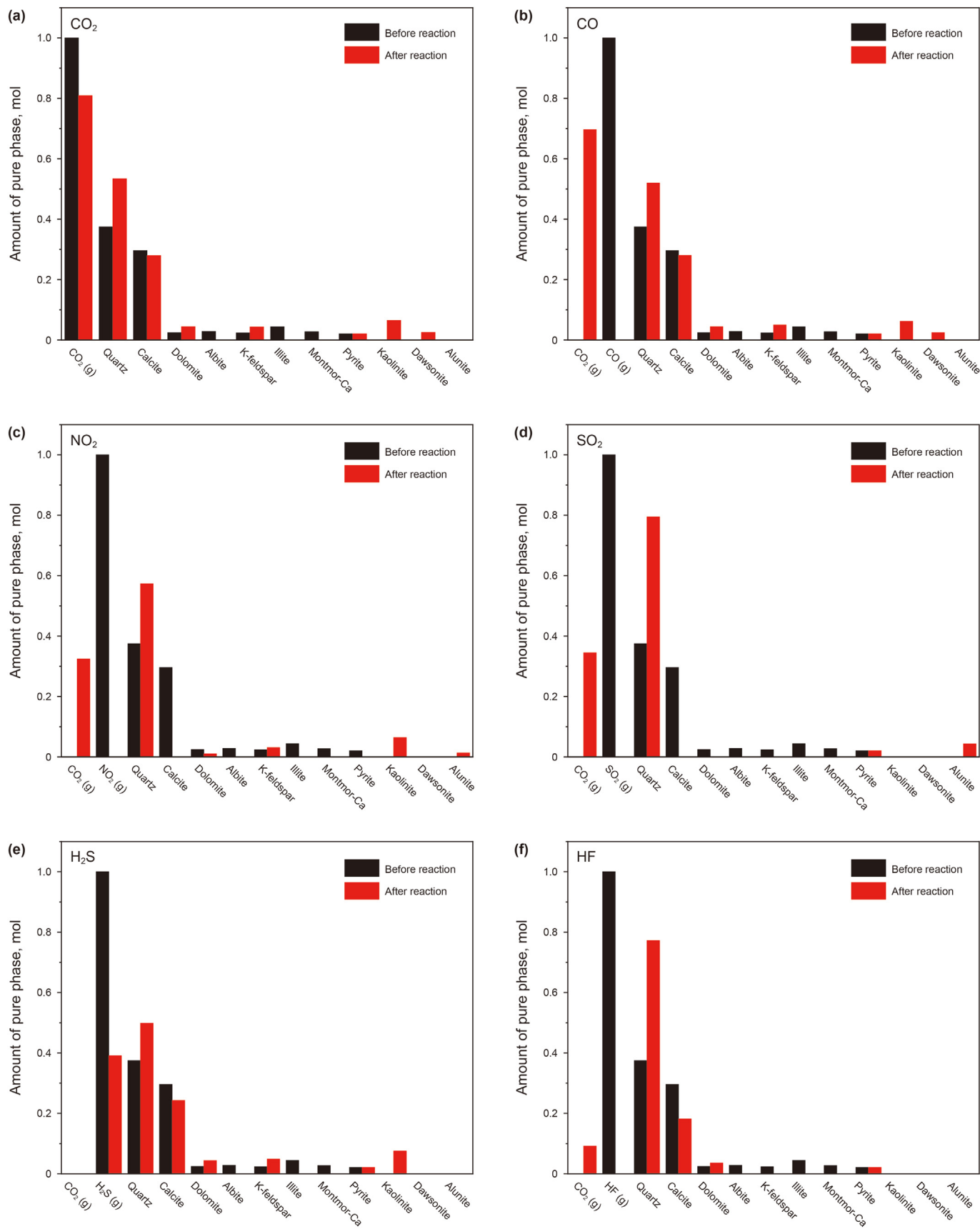
Fig. 2. Amount of each CO_2-rich IWG and shale minerals before and after the reaction. (**a**) CO_2; (**b**) CO; (**c**) NO_2; (**d**) SO_2; (**e**) H_2S; (**e**) HF.
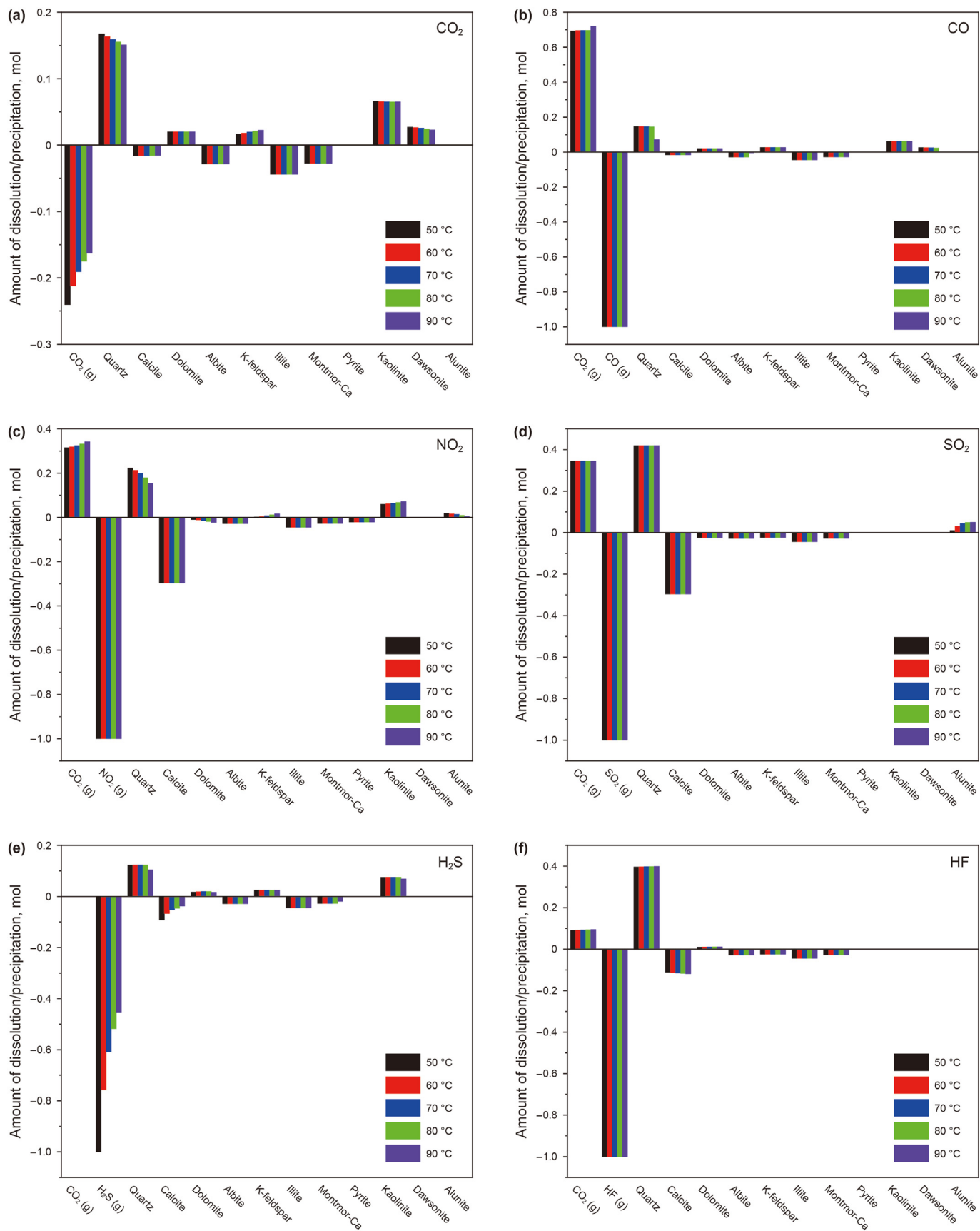
Fig. 3. Amount of dissolution/precipitation on single gas and minerals at different temperatures. (**a**) CO_2; (**b**) CO; (**c**) NO_2; (**d**) SO_2; (**e**) H_2S; (**e**) HF.
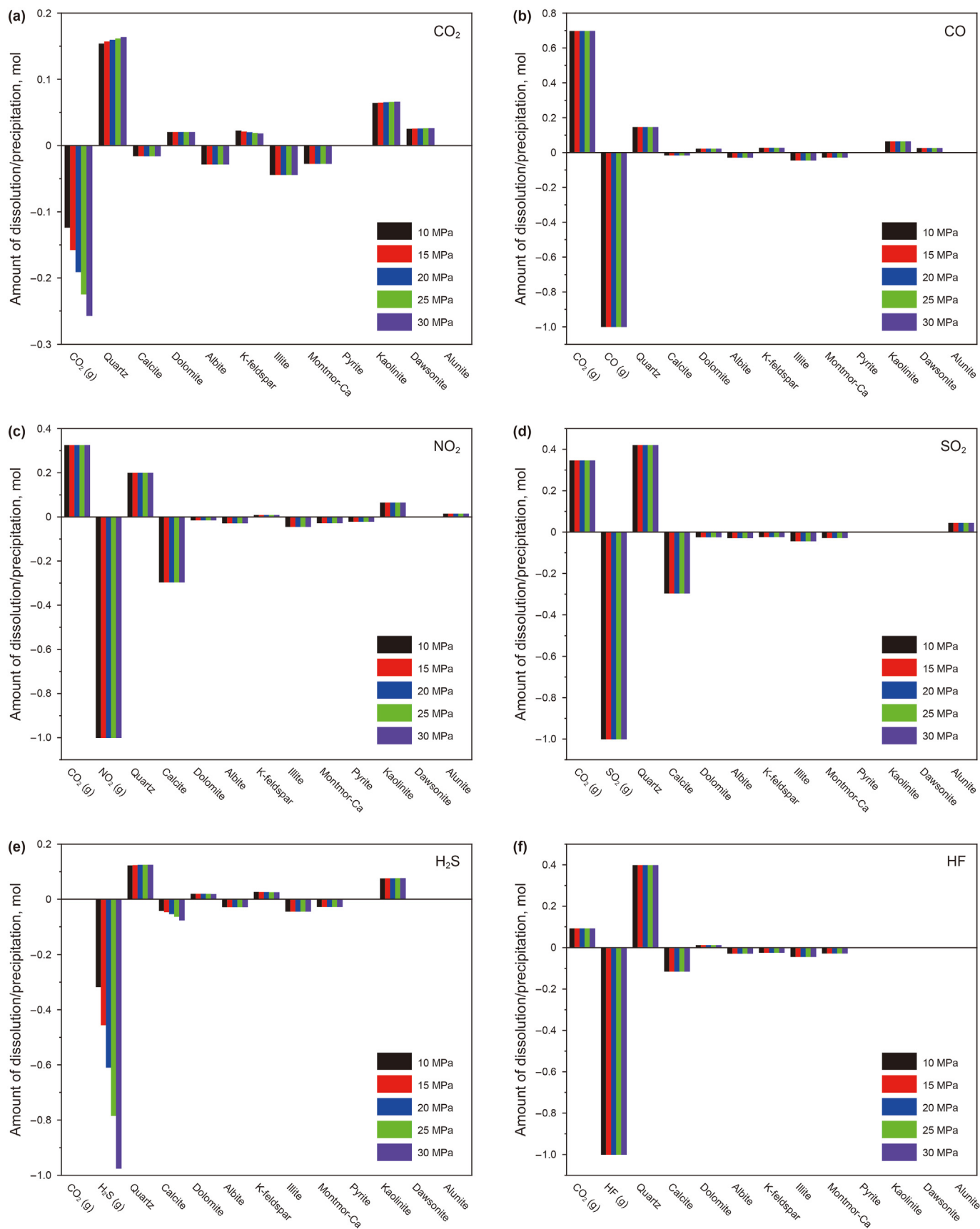
Fig. 4. Amount of dissolution/precipitation on single gas and minerals at different pressures. (**a**) CO_2; (**b**) CO; (**c**) NO_2; (**d**) SO_2; (**e**) H_2S; (**e**) HF.
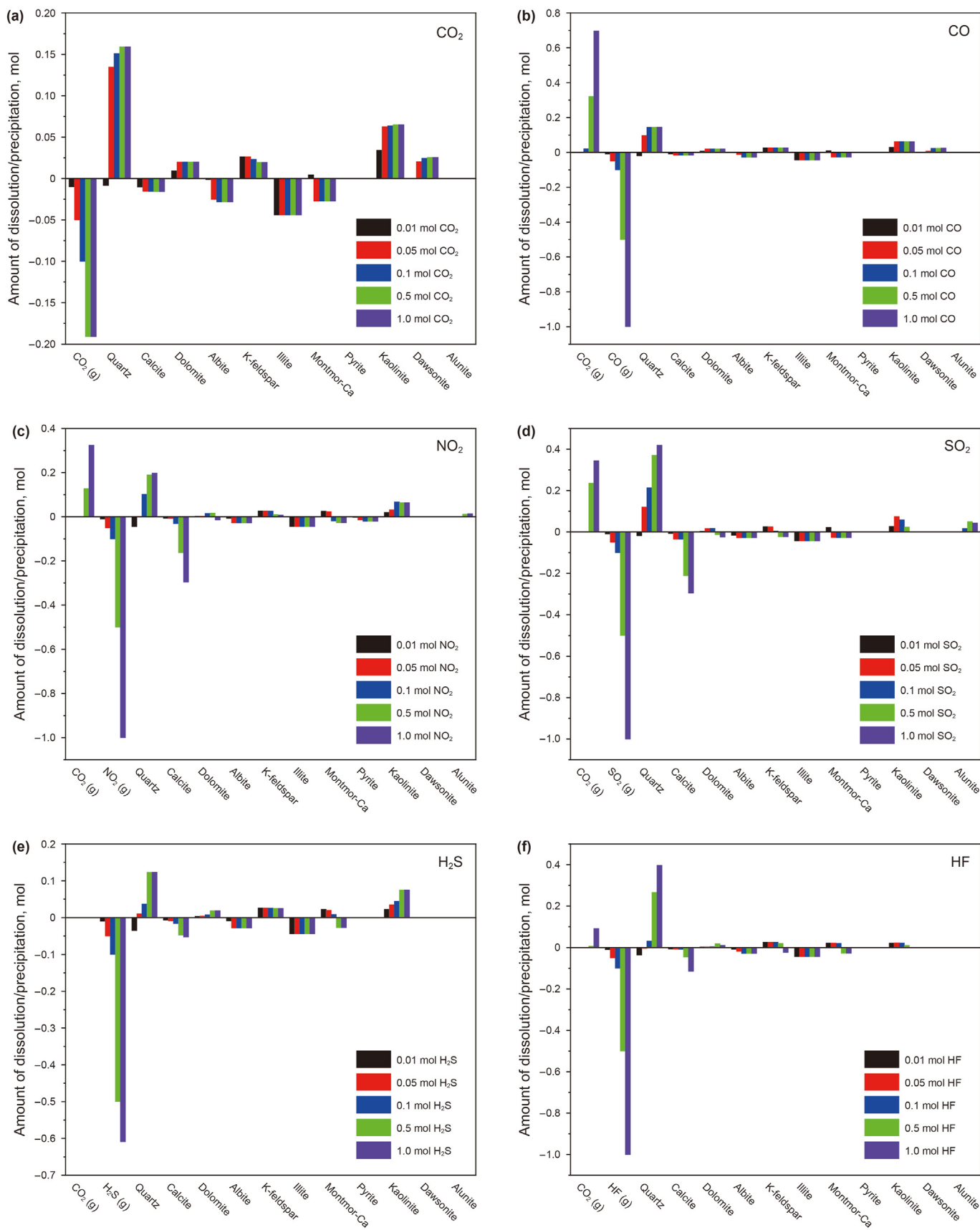
Fig. 5. Amount of dissolution/precipitation on single gas and minerals at different gas concentrations. (**a**) CO_2; (**b**) CO; (**c**) NO_2; (**d**) SO_2; (**e**) H_2S; (**e**) HF.

results reveal that the initial CO_2 amount of 0.75 mol decreased by 12% to 0.66 mol after reaction at the simulated temperature and pressure conditions. Furthermore, the industrial waste gases were entirely consumed, indicating that the storage of CO_2-rich IWG in shale reservoirs through dissolution and chemical reactions is feasible. As for the shale minerals, the simulation results demonstrate that albite, illite, and montmorillonite were entirely dissolved under the simulated conditions, while calcite and K-feldspar were partially dissolved, and quartz, dolomite, secondary minerals such as kaolinite, dawsonite, and alunite were precipitated. The content of pyrite exhibited negligible change after reaction. Compared to the previous studies, which mostly show the reaction of pure CO_2 with rock minerals (Farquhar et al., 2015; Fatah et al., 2021, 2022), the reaction produced alumite due to the presence of SO_2 as well as H_2S in the CO_2-rich IWG.

The thermodynamic equilibrium results of CO_2-rich IWG−water−shale minerals at different temperatures, pressures, gas compositions, and water content are shown in Fig. 7. Based on the results, it can be concluded that the decrease in temperature, increase in pressure, increase in IWG content in the gas mixture and increase in water content under the simulated conditions will increase the dissolved amount of CO_2 and thus promote the acid rock reaction (Zhu et al., 2019; Liu et al., 2019). Besides, CO, NO_2, SO_2, and HF are completely consumed under the simulated conditions, while H_2S is partially dissolved at lower pressure, IWG content, and water content, which shows that under the usual geological storage conditions of CO_2-rich IWG in shale formations, it is feasible to treat and storage IWG by water−rock reaction. As for shale minerals, the dissolution of K-feldspar by CO_2-rich IWG slightly decreases with increasing temperature, while the precipitation of quartz and albite significantly decreases, and the precipitation of kaolinite increases. Increasing pressure promotes the dissolution of K-feldspar and generates precipitation of quartz and albite. Increasing the content of industrial waste gases in the mixed gas promotes the dissolution of K-feldspar, calcite, and kaolinite and generates precipitation of quartz and alunite. The effect of water content is more special, many minerals, such as quartz, calcite, dolomite, K-feldspar, and alunite, exhibit precipitation at low water content, followed by dissolution at higher water content.
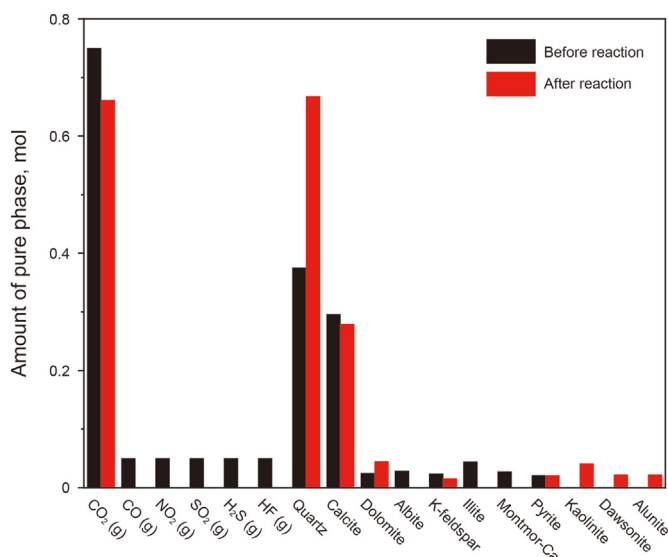
3.1.4. Reaction mechanism of mixed gas−water−shale minerals

When the CO_2 concentration in the CO_2-rich IWG reaches a high level (95%), the concentrations and partial pressures of other gases are low. Consequently, the results of the mixed gas−water−rock reaction with shale minerals are comparable to those of the CO_2 (Fatah et al., 2021, 2022). Specifically, albite, illite, montmorillonite, and some calcite dissolve, while quartz, K-feldspar, and calcite precipitate. Additionally, secondary minerals such as kaolinite, dawsonite, and alunite are generated. Compared to the CO_2−water−rock reaction, the consumption of CO_2 reduces due to the dissolution of NO_2, SO_2, and HF gases and the conversion of CO gas. Furthermore, SO_2 addition results in the formation of secondary minerals containing sulfur, such as alunite. As the industrial waste gas content in the CO_2-rich IWG increases, the acidity of the aqueous solution gradually rises, leading to a significant decrease in CO_2 consumption. When the industrial waste gas content reaches a high level (50%), the generation of CO_2 occurs. This phenomenon is mainly due to the high carbonate (calcite dominated) content of the shale samples selected in this study. Since industrial waste gas is more acidic when dissolved in water, when the industrial waste gas content is high, the concentration of hydrogen ions in the solution is higher. Calcite reacts with hydrogen ions to produce a large amount of bicarbonate, thus reversing the hydrolysis of CO_2 and producing CO_2. In addition, CO gas is not converted into carbonate ions or bicarbonate ions, but only undergoes redox reactions to produce CO_2, which leads to the production of CO_2. Regarding shale minerals, as the industrial waste gas content increases, the dissolution of calcite and K-feldspar increases, and the final precipitation of kaolinite and dawsonite decreases. Meanwhile, the precipitation of quartz and alunite increases. This outcome occurs due to the increase in the acidity of aqueous solutions, which promotes water−rock reactions (Liu et al., 2019; Zhu et al., 2019), resulting in the dissolution of more calcite, K-feldspar, kaolinite, and dawsonite and the formation of more quartz and alunite.

3.2. Effect on shale reservoir physical properties

The variations of reservoir rock skeleton volume after water−rock reaction with temperature, pressure and water content are shown in Fig. 8. Most existing studies suggest that the CO_2−water−rock reaction leads to increased porosity of reservoir rocks, which is detrimental to the stability of CO_2 geological storage (Zou et al., 2018; Liu et al., 2019; Lee et al., 2019), but some studies have obtained the opposite result (Xu et al., 2019; Zhu et al., 2019; Yang et al., 2020). In this study, it can be seen that in the simulated temperature and pressure ranges, the volume of reservoir rock skeleton after water−rock reaction becomes larger, which means that the water−rock reaction is mainly precipitation at this time, and the porosity and permeability of the reservoir rock decrease. With the increase in temperature, the volume change of reservoir rock skeleton volume first decreases and then flattens out, which is due to the fact that the increase in temperature inhibits the dissolution of gas in water, which leads to the decrease in hydrogen ion concentration in the aqueous solution and inhibits the chemical reaction between hydrogen ion and minerals. Since the water−rock reaction is dominated by precipitation under the reaction conditions of this paper, the inhibition of the water−rock reaction leads to a decrease in the amount of mineral precipitation and thus a decrease in the amount of change in the volume of the reservoir rock skeleton. As the pressure increases, the volume of reservoir rock skeleton first increases and then level off. The reason is similar to the effect of temperature, as the pressure increases, the dissolved amount of gas increases, therefore it will promote the water−rock reaction, leading to increases in mineral precipitation and reservoir rock skeleton volume.
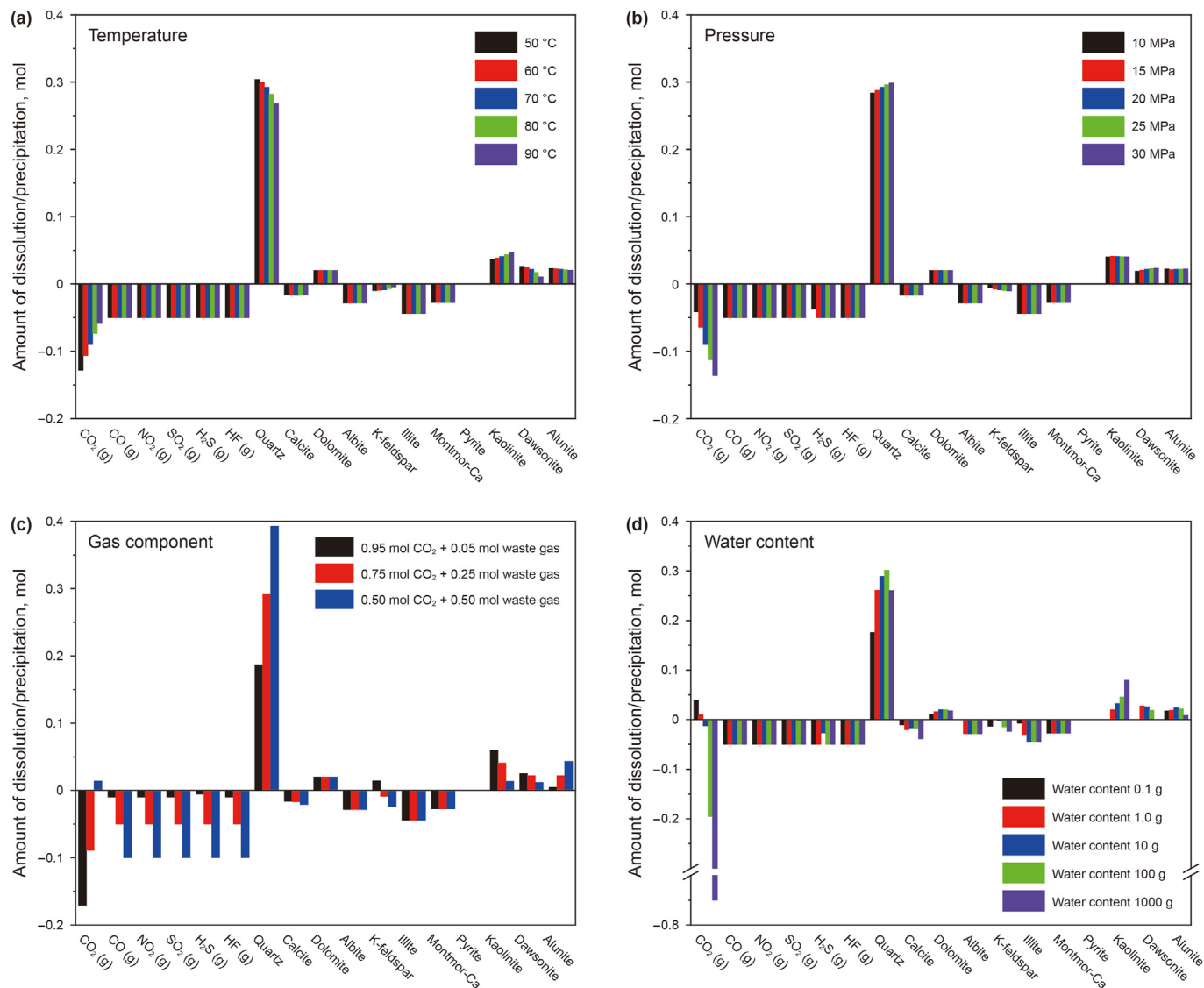

Fig. 6. Amount of CO_2-rich IWG and shale minerals before and after the reaction.

Fig. 7. Amount of dissolution/precipitation on mixed gas and minerals at different conditions. (**a**) Temperature; (**b**) Pressure; (**c**) Gas component; (**d**) Water content.

Existing studies of CO_2−water−rock reactions on reservoir properties rarely involve the effect of water content. The effect of water content on the physical properties of reservoir rocks is different from those of temperature and pressure. The findings demonstrate that, within the simulated temperature and pressure ranges, as the amount of water increases, the volume change of the reservoir rock skeleton first increases and then decreases. Specifically, the volume of the reservoir rock skeleton initially decreases, followed by an increase, and then a decrease again after the water−rock reaction. This implies that the water−rock reaction initially involves dissolution, then precipitation, and finally dissolution again. Correspondingly, the porosity and permeability of the reservoir rock increase, decrease, and then increase again. The observed trend can be attributed to the fact that, with an increase in water volume, acidic gases can dissolve more readily, thereby promoting water−rock reaction (Liu et al., 2019; Zhu et al., 2019). Hence, when the reservoir contains less water, water−rock reactions are primarily dominated by dissolution. During this stage, the hydrogen ions in the aqueous solution react with shale minerals, resulting in a small content of precipitation. As the water content in the reservoir increases, the number of hydrogen ions

participating in the reaction gradually increases. At this stage, the metal cations produced by the dissolution of shale minerals react with the acid anions generated by the hydrolysis of acidic gases to form a considerable content of precipitation. Consequently, precipitation becomes the predominant type of water−rock reaction during this phase. However, as the water content in the reservoir continues to increase, the newly formed mineral precipitates gradually dissolve. Consequently, the volume change of the reservoir rock skeleton after the reaction gradually decreases. Eventually, the volume of the reservoir rock skeleton decreases, and the porosity of the reservoir rock increases. This outcome is unfavorable for the stability of the geological storage of CO_2-rich IWG.

4. Conclusions

In this study, a one-dimensional chemical reaction thermodynamic equilibrium model of the core scale was established. The model was used to simulate the interaction between CO_2-rich IWG and shale to reveal the reaction mechanism between them and explore the impact of this reaction on reservoir properties. Based on the experimental data, several innovative insights were obtained.
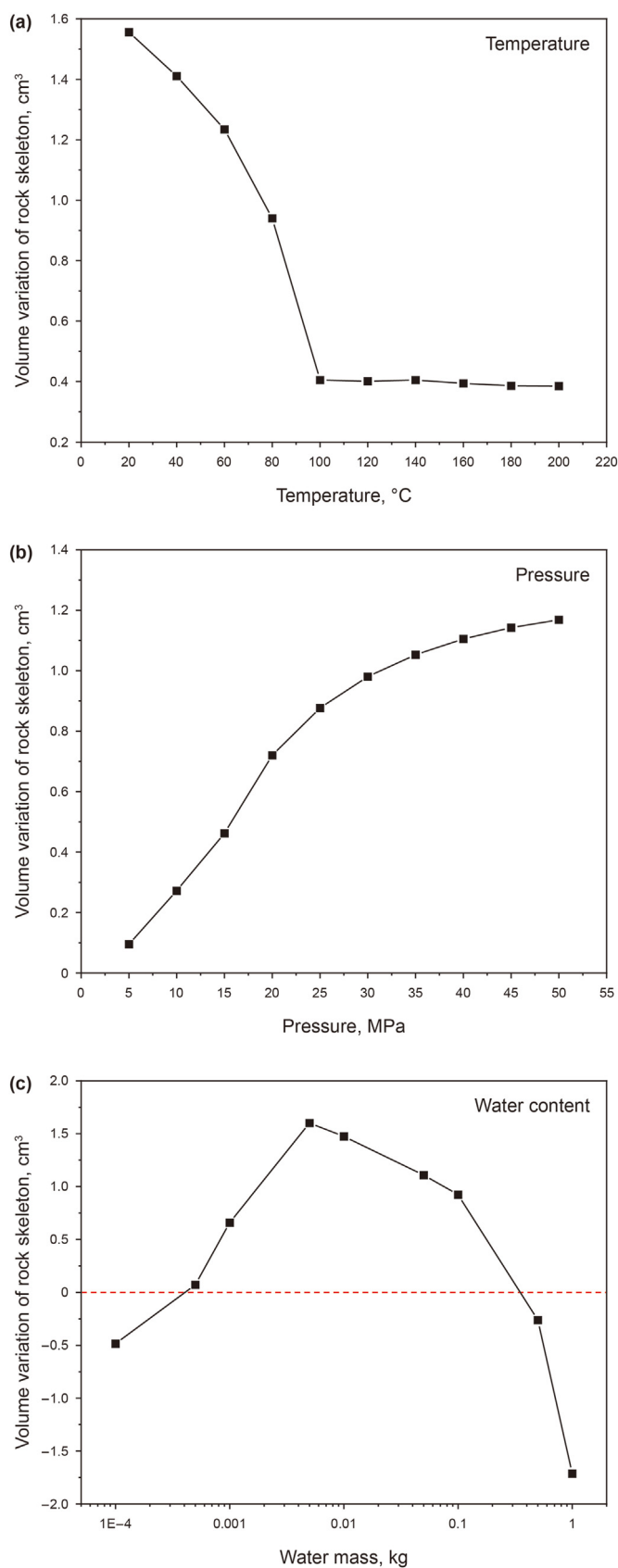
Fig. 8. Effects on volume change of reservoir rock skeleton after reaction. (**a**) Temperature; (**b**) Pressure; (**c**) Water content.

(1) The injection of CO_2, NO_2, SO_2, H_2S, and HF into shale formations leads to their dissolution in water, resulting in the generation of acids and subsequent mineral dissolution and precipitation. The final outcome of this reaction depends on the solubility of the gas and the acidity of the acid. Although CO has low solubility in water, it can undergo oxidation to produce CO_2, leading to a similar reaction mechanism as CO_2.

(2) The dissolution of CO_2 and H_2S in water results in weak acidity, leading to the complete dissolution of albite, illite, and montmorillonite and the eventual generation of quartz and some secondary minerals. Conversely, when SO_2, NO_2, and HF are dissolved in water, they produce strong acidity and can dissolve calcite, dolomite, K-feldspar, and some secondary minerals. Following this reaction, a significant amount of CO_2 is generated.

(3) The presence of IWG can inhibit the dissolution of CO_2 when CO_2-rich IWG reacts with shale. In certain conditions, these gases may even generate CO_2. Therefore, the optimal composition of CO_2-rich IWG is 95% CO_2 and 5% IWG when CO_2 geological storage is the main goal, and that 19% of the initial amount of CO_2 is consumed after the water−rock reaction under these conditions. In contrast, when the main goal is the geological storage of total CO_2-rich IWG or impurity gas, the optimal CO_2-rich IWG composition is 50% CO_2 and 50% IWG, with 48% of the initial amount of CO_2-rich IWG consumed after the reaction. Under simulated temperature and pressure conditions, CO_2 consumed 12% after reaction, CO, NO_2, SO_2, and HF gases dissolve completely in water, while H_2S can dissolve mostly under most temperature and pressure conditions, with a small portion remaining undissolved. Therefore, geological storage of industrial waste gas is feasible.

(4) In the CO_2-rich IWG−water−shale reaction, temperature has less influence on the water−rock reaction, while pressure is the most important parameter. On the one hand, the pressure varies greatly from one reservoir to another. On the other hand, the pressure not only affects the amounts of various gases dissolved in the formation water, thus affecting the reaction process of the acid rock reaction, but also affects the total amount of injected gases, which has a significant impact on the results of the CO_2-rich IWG−water−shale reaction. In addition, it can be seen from Fig. 3 that SO_2 has the greatest impact on the acid−rock reaction in gas. For minerals, clay minerals such as illite and montmorillonite were involved in the reaction in high amounts and at faster rates, which had a significant effect on the results of the acid−rock reaction.

(5) The overall reaction is dominated by precipitation and the volume of the rock skeleton has increased by 0.74 cm^3, resulting in a decrease in shale porosity. Under simulated temperature and pressure conditions, the water−rock reaction is dominated by precipitation, with the change in reservoir rock volume first decreasing and then gradually becoming flat with increasing temperature and first increasing and then gradually becoming stable with increasing pressure. As the water content of the reservoir increases, the water−rock reaction first dissolves, then precipitates, and then dissolves again. When the water content is less than 0.0005 kg or greater than 0.4 kg, it will lead to an increase in reservoir porosity, thereby affecting the stability of long-term geological storage of CO_2-rich IWG.

Declaration of competing interest

The authors declare that they have no known competing

financial interests or personal relationships that could have appeared to influence the work reported in this paper.

References

Aminu, M.D., Nabavi, S.A., Manovic, V., 2018. CO$_2$-brine-rock interactions: the effect of impurities on grain size distribution and reservoir permeability. Int. J. Greenh. Gas Control 78, 168–176. https://doi.org/10.1016/j.ijggc.2018.08.008.

Ao, X., Lu, Y., Tang, J., Chen, Y., Li, H., 2017. Investigation on the physics structure and chemical properties of the shale treated by supercritical CO$_2$. J. CO$_2$ Util. 20, 274–281. https://doi.org/10.1016/j.jcou.2017.05.028.

Bethke, C.M., 1996. Geochemical Reaction Modelling: Concepts and Applications. Oxford University Press, USA. https://doi.org/10.1093/oso/9780195094756.001.0001.

Bhuiyan, M.H., Agofack, N., Gawel, K.M., Cerasi, P.R., 2020. Micro- and macroscale consequences of interactions between CO$_2$ and shale rocks. Energies 13 (5), 1167. https://doi.org/10.3390/en13051167.

Cheng, Y., Zeng, M., Lu, Z., Du, X., Yin, H., Yang, L., 2020. Effects of supercritical CO$_2$ treatment temperatures on mineral composition, pore structure and functional groups of shale: implications for CO$_2$ sequestration. Sustainability 12 (9), 3927. https://doi.org/10.3390/su12093927.

Dai, X., Wang, M., Wei, C., Zhang, J., Wang, X., Zou, M., 2020. Factors affecting shale microscopic pore structure variation during interaction with supercritical CO$_2$. J. CO$_2$ Util. 38, 194–211. https://doi.org/10.1016/j.jcou.2020.01.021.

Davies, J.T., 1951. The distribution of ions under a charged monolayer, and a surface equation of state for charged films. Proc. Roy. Soc. Lond. 208 (1093), 224–247. https://doi.org/10.2307/98714.

Dong, D., Shi, Z., Sun, S., Guo, C., Zhang, C., Guo, W., Guan, Q., Zhang, M., Jiang, S., Zhang, L., Ma, C., Wu, J., Li, N., Chang, Y., 2018. Factors controlling microfractures in black shale: a case study of ordovician wufeng formation-silurian Longmaxi Formation in shuanghe profile, changning area, Sichuan Basin, SW China. Petrol. Explor. Dev. 45 (5), 818–829. https://doi.org/10.1016/S1876-3804(18)30085-5.

Farquhar, S.M., Pearce, J.K., Dawson, G.K., Golab, A., Sommacal, S., Kirste, D., Biddle, D., Golding, S.D., 2015. A fresh approach to investigating CO$_2$ storage: experimental CO$_2$-water-rock interactions in a low-salinity reservoir system. Chem. Geol. 399, 98–122. https://doi.org/10.1016/j.chemgeo.2014.10.006.

Fatah, A., Ben Mahmud, H., Bennour, Z., Hossain, M., Gholami, R., 2021. Effect of supercritical CO$_2$ treatment on physical properties and functional groups of shales. Fuel 303, 121310. https://doi.org/10.1016/j.fuel.2021.121310.

Fatah, A., Bennour, Z., Ben Mahmud, H., Gholami, R., Hossain, M.M., 2020. A review on the influence of CO$_2$/shale interaction on shale properties: implications of CCS in shales. Energies 13 (12), 3200. https://doi.org/10.3390/en13123200.

Fatah, A., Mahmud, H.B., Bennour, Z., Gholami, R., Hossain, M., 2022. The impact of supercritical CO$_2$ on the pore structure and storage capacity of shales. J. Nat. Gas Sci. Eng. 98, 104394. https://doi.org/10.1016/j.jngse.2021.104394.

Garrels, R.M., Christ, C.L., 1965. Solutions, Minerals and Equilibria. Harper and Row, New York, p. 450.

Ghayur, A., Verheyen, T.V., Meuleman, E., 2019. Biological and chemical treatment technologies for waste amines from CO$_2$ capture plants. J. Environ. Manag. 241, 514–524. https://doi.org/10.1016/j.jenvman.2018.07.033.

Hadian, P., Rezaee, R., 2019. The effect of supercritical CO$_2$ on shaly caprocks. Energies 13 (1), 149. https://doi.org/10.3390/en13010149.

Hu, Y., Hao, M., Chen, G., Sun, R., Li, S., 2019. Technologies and practice of CO$_2$ flooding and sequestration in China. Petrol. Explor. Dev. 46 (4), 753–766. https://doi.org/10.1016/S1876-3804(19)60233-8.

Hui, D., Pan, Y., Luo, P., Zhang, Y., Sun, L., Lin, C., 2019. Effect of supercritical CO$_2$ exposure on the high-pressure CO$_2$ adsorption performance of shales. Fuel 247, 57–66. https://doi.org/10.1016/j.fuel.2019.03.013.

IEA., 2022. Global Energy Review: CO$_2$ Emissions in 2021. International Energy Agency, Paris. https://www.iea.org/reports/global-energy-review-2021.

Ilgen, A.G., Aman, M., Espinoza, D.N., Rodriguez, M.A., Griego, J.M., Dewers, T.A., Feldman, J.D., Stewart, T.A., Choens, R.C., Wilson, J., 2018. Shale-brine-CO$_2$ interactions and the long-term stability of carbonate-rich shale caprock. Int. J. Greenh. Gas Control 78, 244–253. https://doi.org/10.1016/j.ijggc.2018.07.002.

Klajmon, M., Havlova, V., Cervinka, R., Mendoza, A., Francu, J., Berenblyum, R., Arild, O., 2017. REPP-CO$_2$: equilibrium modelling of CO$_2$-rock-brine systems. Energy Proc. 144, 3364–3373. https://doi.org/10.1016/j.egypro.2017.03.1468.

Koukouzas, N., Kyprianidou, G., Purser, G., Rochelle, C.A., Vasilatos, C., Tsoukalas, N., 2018. Assessment of the impact of CO$_2$ storage in sandstone formations by experimental studies and geochemical modeling: the case of the Mesohellenic Trough, NW Greece. Int. J. Greenh. Gas Control 71, 116–132. https://doi.org/10.1016/j.ijggc.2018.01.016.

Lang, D., Lun, Z., Lyu, C., Wang, H., Zhao, Q., Sheng, H., 2021. Nuclear magnetic resonance experimental study of CO$_2$ injection to enhance shale oil recovery. Petrol. Explor. Dev. 48 (3), 702–712. https://doi.org/10.11698/PED.2021.03.15.

Lee, J.H., Yoo, W., Lee, K.S., 2019. Effects of aqueous solubility and molecular diffusion on CO$_2$-enhanced hydrocarbon recovery and storage from liquid-rich shale reservoirs. Energy Sources 41 (10), 1230–1241. https://doi.org/10.1080/15567036.2018.1545000.

Li, X., Wang, A., Yu, W., 2010. A trend analysis of carbon dioxide emissions based on the energy demand. Acta Geosci. Sin. 31 (5), 741–748. https://doi.org/10.3975/cagsb.2010.05.19.

Li, Y., Wang, R., Zhao, Q., Xue, Z., Zhou, Y., 2023. A CO$_2$ storage potential evaluation method for saline aquifers in a petroliferous basin. Petrol. Explor. Dev. 50 (2), 484–491. https://doi.org/10.1016/S1876-3804(23)60403-3.

Liao, G., He, D., Wang, G., Wang, L., Wang, Z., Su, C., Qin, Q., Bai, J., Hu, Z., Huang, Z., Wang, J., Wang, S., 2022. Discussion on the limit recovery factor of carbon dioxide flooding in a permanent sequestration scenario. Petrol. Explor. Dev. 49 (6), 1463–1470. https://doi.org/10.1016/S1876-3804(23)60364-7.

Liu, B., Zhao, F., Xu, J., Qi, Y., 2019. Experimental investigation and numerical simulation of CO$_2$-brine-rock interactions during CO$_2$ sequestration in a deep saline aquifer. Sustainability 11 (2), 1–17. https://doi.org/10.3390/su11020317.

Liu, D., Li, Y., Agarwal, R.K., 2016. Numerical simulation of long-term storage of CO$_2$ in Yanchang shale reservoir of the Ordos basin in China. Chem. Geol. 440, 288–305. https://doi.org/10.1016/j.chemgeo.2016.08.002.

Lyu, Q., Long, X., Ranjith, P.G., Tan, J., Kang, Y., Wang, Z., 2018. Experimental investigation on the mechanical properties of a low-clay shale with different adsorption times in sub-/super-critical CO$_2$. Energy 147, 1288–1298. https://doi.org/10.1016/j.energy.2018.01.084.

Merey, S., Sinayuc, C., 2016. Analysis of carbon dioxide sequestration in shale gas reservoirs by using experimental adsorption data and adsorption models. J. Nat. Gas Sci. Eng. 36, 1087–1105. https://doi.org/10.1016/j.jngse.2016.02.052.

Middleton, R.S., Carey, J.W., Currier, R.P., Hyman, J.D., Kang, Q., Karra, S., Jimenez-Martinez, J., Porter, M.L., Viswanathan, H.S., 2015. Shale gas and non-aqueous fracturing fluids: opportunities and challenges for supercritical CO$_2$. Appl. Energy 147, 500–509. https://doi.org/10.1016/j.apenergy.2015.03.023.

Pan, B., Gong, C., Wang, X., Li, Y., Iglauer, S., 2020. The interfacial properties of clay-coated quartz at reservoir conditions. Fuel 262, 116461. https://doi.org/10.1016/j.fuel.2019.116461.

Pan, Y., Hui, D., Luo, P., Zhang, Y., Sun, L., Wang, K., 2018. Experimental investigation of the geochemical interactions between supercritical CO$_2$ and shale: implications for CO$_2$ storage in gas-bearing shale formations. Energy Fuel. 32 (2), 1963–1978. https://doi.org/10.1021/acs.energyfuels.7b03074.

Pearce, J.K., Dawson, G.K.W., Law, A.C.K., Biddle, D., Golding, S.D., 2016. Reactivity of micas and cap-rock in wet supercritical CO$_2$ with SO$_2$ and O$_2$ at CO$_2$ storage conditions. Appl. Geochem. 72, 59–76. https://doi.org/10.1016/j.apgeochem.2016.06.010.

Pearce, J.K., Khan, C., Golding, S.D., Rudolph, V., Underschultz, J.R., 2022. Geological storage of CO$_2$ and acid gases dissolved at surface in production water. J. Pet. Sci. Eng. 210, 110052. https://doi.org/10.1016/j.petrol.2021.110052.

Qin, C., Jiang, Y., Luo, Y., Zhou, J., Liu, H., Song, X., Li, D., Zhou, F., Xie, Y., 2020. Effect of supercritical CO$_2$ saturation pressures and temperatures on the methane adsorption behaviours of Longmaxi shale. Energy 206, 118150. https://doi.org/10.1016/j.energy.2020.118150.

Rezaee, R., Saeedi, A., Iglauer, S., Evans, B., 2017. Shale alteration after exposure to supercritical CO$_2$. Int. J. Greenh. Gas Control 62, 91–96. https://doi.org/10.1016/j.ijggc.2017.04.004.

Song, X., Guo, Y., Zhang, J., Sun, N., Shen, G., Chang, X., Yu, W., Tang, Z., Chen, W., Wei, W., Wang, L., Zhou, J., Li, X., Li, X., Zhou, J., Xue, Z., 2019. Fracturing with carbon dioxide: from microscopic mechanism to reservoir application. Joule 3 (8), 1913–1926. https://doi.org/10.1016/j.joule.2019.05.004.

Song, X., Li, G., Guo, B., Wang, H., Li, X., Lu, Z., 2018. Transport feasibility of proppant by supercritical carbon dioxide fracturing in reservoir fractures. J. Hydrodyn. 30 (3), 507–513. https://doi.org/10.1007/s42241-018-0055-0.

Song, X., Wang, F., Ma, D., Gao, M., Zhang, Y., 2023. Progress and prospect of carbon dioxide capture, utilization and storage in CNPC oilfields. Petrol. Explor. Dev. 50 (1), 229–244. https://doi.org/10.1016/S1876-3804(22)60383-5.

Sturmer, D.M., Tempel, R.N., Soltanian, M.R., 2020. Geological carbon sequestration: modeling mafic rock carbonation using point-source flue gases. Int. J. Greenh. Gas Control 99, 103106. https://doi.org/10.1016/j.ijggc.2020.103106.

Sun, X., Nie, H., Su, H., Du, W., Lu, T., Chen, Y., Liu, M., Li, J., 2023. Porosity, permeability and rock mechanics of Lower Silurian Longmaxi Formation deep shale under temperature-pressure coupling in the Sichuan Basin, SW China. Petrol. Explor. Dev. 50 (1), 85–98. https://doi.org/10.1016/S1876-3804(22)60371-9.

Teng, X., Lu, D., Chiu, Y., 2019. Emission reduction and energy performance improvement with different regional treatment intensity in China. Energies 12 (2), 237. https://doi.org/10.3390/en12020237.

Turner, L.G., Dawson, G.K.W., Golding, S.D., Pearce, J.K., 2022. CO$_2$ and NO$_x$ reactions with CO$_2$ storage reservoir core: NO$_x$ dissolution products and mineral reactions. Int. J. Greenh. Gas Control 120, 103750. https://doi.org/10.1016/j.ijggc.2022.103750.

Wang, G., 2023. Carbon dioxide capture, enhanced-oil recovery and storage technology and engineering practice in Jilin Oilfield, NE China. Petrol. Explor. Dev. 50 (1), 245–254. https://doi.org/10.1016/S1876-3804(22)60384-7.

Wang, H., Shi, Z., Sun, S., 2021. Biostratigraphy and reservoir characteristics of the ordovician wufeng-silurian Longmaxi shale in the Sichuan Basin and surrounding areas, China. Petrol. Explor. Dev. 48 (5), 879–890. https://doi.org/10.1016/S1876-3804(21)60088-5.

Wang, J., Bai, H., Wang, S., Ji, Z., Liu, H., 2022a. Feasibility study on using CO$_2$-rich

industrial waste gas replacement for shale gas exploration based on adsorption characteristics. Chem. Eng. J. 443, 136386. https://doi.org/10.1016/j.cej.2022.136386.

Wang, J., Bai, H., Wang, S., Liu, R., Ji, Z., Liu, H., Omara, E.R., 2022b. Feasibility study on CO_2-rich industrial waste gas storage and replacement in carbonate gas reservoir based on adsorption characteristics. J. Petrol. Sci. Eng. 217, 110938. https://doi.org/10.1016/j.petrol.2022.110938.

Wang, J., Wang, Z., Sun, B., Gao, Y., Wang, X., Fu, W., 2019. Optimization design of hydraulic parameters for supercritical CO_2 fracturing in unconventional gas reservoir. Fuel 235, 795−809. https://doi.org/10.1016/j.fuel.2018.08.078.

Xu, T., Zhu, H., Feng, G., Yang, Z., Tian, H., 2019. Numerical simulation of calcite vein formation and its impact on caprock sealing efficiency - case study of a natural CO_2 reservoir. Int. J. Greenh. Gas Control 83, 29−42. https://doi.org/10.1016/j.ijggc.2019.01.021.

Yang, G., Ma, X., Feng, T., Yu, Y., Yin, S., Huang, M., Wang, Y., 2020. Geochemical modelling of the evolution of caprock sealing capacity at the shenhua CCS demonstration project. Minerals 10 (11), 1009. https://doi.org/10.3390/min10111009.

Yin, H., Zhou, J., Jiang, Y., Xian, X., Liu, Q., 2016. Physical and structural changes in shale associated with supercritical CO_2 exposure. Fuel 184, 289−303. https://doi.org/10.1016/j.fuel.2016.07.028.

Yuan, S., Ma, D., Li, J., Zhou, T., Ji, Z., Han, H., 2022. Progress and prospects of carbon dioxide capture, EOR-utilization and storage industrialization. Petrol. Explor. Dev. 49 (4), 955−962. https://doi.org/10.1016/S1876-3804(22)60324-0.

Yuan, Z., Liao, X., Zhang, K., Zhao, X., Chen, Z., 2021. The effect of inorganic salt precipitation on oil recovery during CO_2 flooding: a case study of Chang 8 block in Changqing oilfield, NW China. Petrol. Explor. Dev. 48 (2), 442−449. https://doi.org/10.1016/S1876-3804(21)60035-6.

Zhang, J., Liu, J., Dong, L., Qiao, Q., 2022. CO_2 Emissions inventory and its uncertainty analysis of China's industrial parks: a case study of the maanshan economic and technological development area. Int. J. Environ. Res. Publ. Health 19 (18), 11684. https://doi.org/10.3390/ijerph191811684.

Zhang, T., Li, Y., Li, Y., Sun, S., Gao, X., 2020b. A self-adaptive deep learning algorithm for accelerating multi-component flash calculation. Comput. Methods Appl. Mech. Eng. 369, 113207. https://doi.org/10.1016/j.cma.2020.113207.

Zhang, T., Li, Y., Sun, S., Bai, H., 2020a. Accelerating flash calculations in unconventional reservoirs considering capillary pressure using an optimized deep learning algorithm. J. Petrol. Sci. Eng. 195 (6), 107886. https://doi.org/10.1016/j.petrol.2020.107886.

Zhou, J., Hu, N., Xian, X., Zhou, L., Tang, J., Kang, Y., Wang, H., 2019. Supercritical CO_2 fracking for enhanced shale gas recovery and CO_2 sequestration: results, status and future challenges. Adv.Geo-Energy Res. 3 (2), 207−224. https://doi.org/10.26804/ager.2019.02.10.

Zhou, J., Yang, K., Tian, S., Zhou, L., Xian, X., Jiang, Y., Liu, M., Cai, J., 2020. CO_2-water-shale interaction induced shale microstructural alteration. Fuel 263, 116642. https://doi.org/10.1016/j.fuel.2019.116642.

Zhou, X., Su, Z., Chen, H., Xiao, X., Qin, Y., Yang, L., Yan, Z., Sun, W., 2018. Capture of pure toxic gases through porous materials from molecular simulations. Mol. Phys. 116 (15−16), 2095−2107. https://doi.org/10.1080/00268976.2018.1440019.

Zhu, H., Xu, T., Tian, H., Feng, G., Yang, Z., Zhou, B., 2019. Understanding of long-term CO_2 -Brine-rock geochemical reactions using numerical modeling and natural analogue study. Geofluids, 1426061. https://doi.org/10.1155/2019/1426061, 2019.

Zou, C., Wu, S., Yang, Z., Pan, S., Wang, G., Jiang, X., Guan, M., Yu, C., Yu, Z., Shen, Y., 2023. Progress, challenge and significance of building a carbon industry system in the context of carbon neutrality strategy. Petrol. Explor. Dev. 50 (1), 210−228. https://doi.org/10.1016/S1876-3804(22)60382-3.

Zou, Y., Li, S., Ma, X., Zhang, S., Li, N., Chen, M., 2018. Effects of CO_2-brine-rock interaction on porosity/permeability and mechanical properties during supercritical-CO_2 fracturing in shale reservoirs. J. Nat. Gas Sci. Eng. 49, 157−168. https://doi.org/10.1016/j.jngse.2017.11.004.